


Cite this: *Energy Adv.*, 2024,
3, 1414Received 20th March 2024,
Accepted 3rd May 2024

DOI: 10.1039/d4ya00184b

rsc.li/energy-advances

Iridium complex modified MOFs for enhancing photocatalytic hydrogen evolution†

Yue Wang,^{ab} Yifan Huang,^{ab} Shihan Liu,^{ab} Shuaichuan Cui,^{ab} Yifan Zhang^{*ab} and
Pengyang Deng ^{*ab}

In this paper, we prepared an iridium(III) complex modified MOF (cmrIr/Pt@UiO-66-NH₂) to combine the excellent light absorption properties of iridium(III) complexes and good photostability of metal-organic frameworks (MOFs). Photocatalytic tests show that even with extremely low content of cmrIr, cmrIr/Pt@UiO-66-NH₂ achieves enhanced hydrogen evolution performance while maintaining the inherent photostability of the MOF. The hydrogen evolution amount of cmrIr/Pt@UiO-66-NH₂ (with only 0.2% of Ir content) is 446.4 $\mu\text{mol g}^{-1}$, which is about 2.5 times that of Pt@UiO-66-NH₂ (180.7 $\mu\text{mol g}^{-1}$). Solid UV, photocurrent response and electrochemical impedance tests indicate that the introduction of the iridium(III) complex promotes the separation of electrons and holes, thus sensitizing the MOF and resulting in enhanced photocatalytic activity. This study provides a new insight for the design of hybrid material photocatalysts.

Introduction

Hydrogen energy is a clean, sustainable secondary energy source and an ideal candidate to replace fossil fuels and solve the energy crisis and environmental pollution.^{1–6} Photocatalytic water splitting harnesses nature's abundant solar and water resources and converts them into chemical energy, a promising way of obtaining hydrogen energy cheaply.^{7–12}

Metal-organic framework (MOF) materials, especially the classical UiO-66-NH₂, are considered promising photocatalysts due to their large specific surface area, tunable pore structure and functionality.^{3,13–23} The ordered structure and high crystallinity of MOFs give them a unique advantage in charge transfer.^{24,25} However, the wider energy bands and shorter photogenerated carrier lifetimes have hindered their further development and application; for example, the photocatalytic activity of the classical UiO-66-NH₂ is extremely low (only 1.72 $\mu\text{mol g}^{-1} \text{ h}^{-1}$).²⁶ Currently, metal nanoparticle-loaded cocatalysis and dye sensitization are two effective ways to improve the photocatalytic performance of MOFs.^{27–38} For example, Jiang *et al.* reported UiO-66-NH₂ loaded with platinum nanoparticles, which achieved effective separation of electrons and holes.^{22,26} Wu *et al.* sensitized a MOF with eosin Y, which increased the visible absorption of the material, thus

enhancing its photocatalytic hydrogen production activity.³⁹ Combining photosensitizers (such as iridium(III) complexes) with MOFs is also used for enhancing the photocatalytic performance of the MOFs. Due to the good light-absorbing ability of metallic iridium(III) complexes, they can be used as an antenna to increase the adsorption of light by MOFs. For instance, Zhang *et al.* synthesized the MOF UiO67-Ir-Cou 6 by using an iridium(III) complex with a coumarin 6 moiety as an organic ligand, achieving 109 times the hydrogen evolution activity of the control MOF.⁴⁰ Therefore, the design and synthesis of iridium(III)-based MOF hybrid materials are expected to achieve stable and efficient photocatalytic hydrogen evolution.

In this paper, we designed and synthesized an iridium(III)-modified MOF (cmrIr/Pt@UiO-66-NH₂) by postsynthetic modification. Cationic iridium(III) complex cmrIr, with a coumarin moiety functionalized cyclometallic ligand and a carboxylate group functionalized auxiliary ligand, was used to modify UiO-66-NH₂ loaded with platinum nanoparticles. Coumarin was introduced to increase the absorption of visible light by the iridium(III) complexes, and the carboxylate group was introduced to coordinate with the defects of the MOF. Photocatalytic tests showed that even with an extremely low content of cmrIr, the cmrIr/Pt@UiO-66-NH₂ had good hydrogen evolution activity and stability. This work enriches the variety of iridium based-MOF photocatalysts, and will provide new insights for the design of hybrid material photocatalysts.

Results and discussion

The preparation of cmrIr/Pt@UiO-66-NH₂ is shown in Fig. 1. First, the coumarin-based ligand cmrIr and Pt nanoparticles

^a State Key Laboratory of Polymer Physics and Chemistry, Changchun Institute of Applied Chemistry, Chinese Academy of Sciences, Changchun, 130022, China.

E-mail: yfzhang@ciac.ac.cn, pydeng@ciac.ac.cn

^b School of Applied Chemistry and Engineering, University of Science and Technology of China, Hefei, 230026, China

† Electronic supplementary information (ESI) available. See DOI: <https://doi.org/10.1039/d4ya00184b>

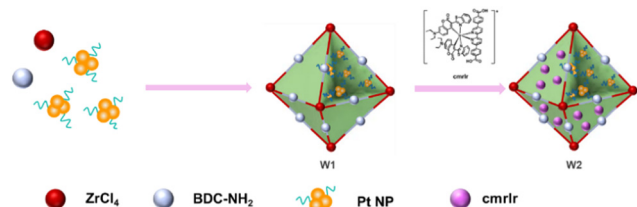


Fig. 1 Scheme for the preparation of $\text{cmrIr/Pt@UiO-66-NH}_2$.

were synthesized. Then, Pt@UiO-66-NH_2 (**W1**) was synthesized by a hydrothermal method and Pt nanoparticles were encapsulated into the cage of UiO-66-NH_2 . Finally, $\text{cmrIr/Pt@UiO-66-NH}_2$ (**W2**) was obtained by modifying cmrIr onto the surface of **W1** (details in the Experimental section). The structure and purity of all synthesized ligands were analyzed using nuclear magnetic resonance hydrogen spectroscopy ($^1\text{H-NMR}$) and matrix-assisted laser desorption ionization time-of-flight mass spectrometry (MALDI-TOF MS) (Fig. S1–S9, ESI †).

The morphology of the Pt nanoparticles, **W1** and **W2**, were characterized using TEM and SEM. As shown in Fig. 2a, the distribution of nanoparticles in the TEM images is relatively uniform. The particle size analysis shows that the particle size of the nanoparticles is distributed in the range of 2–3.5 nm (Fig. 2b). The TEM image of **W1** shows a clear octahedral profile, while Pt nanoparticles encapsulated in the MOF can be observed, which proves that Pt nanoparticles are successfully loaded into the MOF (Fig. 2c). The SEM image of **W1** shows multiple octahedral units with good homogeneity, and the size

of each octahedron is around 200 nm (Fig. 2d). The EDS image shows a uniform distribution of C, H, O, and Zr, which is consistent with the distribution of the MOF units (Fig. S10, ESI †). As shown in Fig. 2e, the SEM image of **W2** is basically the same as **W1**, still showing independent octahedral configurations with good morphology. TEM images of **W2** also show the octahedral structure of **W2** and the encapsulation of Pt nanoparticles inside **W2** (Fig. S11, ESI †), proving that the modification of the MOF by iridium(III) complexes does not affect their morphology. Meanwhile, iridium can be observed in the elemental distribution map (Fig. 2f), and its distribution is consistent with that of **W2**, which proves that iridium is anchored on the surface of the MOF. The platinum element is not detected in the EDS images of either **W1** or **W2**, because EDS detects the elemental distribution on the surface of the samples, whereas the platinum nanoparticles are encapsulated interiorly, and thus cannot be detected. The Ir and Pt contents of **W1** and **W2** are shown in Table S1 (ESI †), the Ir content on **W2** is only 0.24% and the Pt content is 1.41%.

Powder X-ray diffraction (PXRD) was used to investigate the crystal structure of **W1** and **W2**. The PXRD curves of **W1** and **W2** are almost identical (Fig. 3a). Compared with the XRD curves of standard UiO-66 , the diffraction peaks of **W1** and **W2** at 7.36° , 8.48° , and 12.04° correspond to the (111), (002), and (022) crystal planes of UiO-66 , respectively. The XRD results show that both the encapsulation of Pt nanoparticles and the modification of cmrIr do not significantly affect the crystal structure of UiO-66 . The specific surface areas of **W1** and **W2** were also determined. As shown in Fig. 3b, the nitrogen adsorption isotherms for both **W1** and **W2** are type I-type microporous adsorption isotherms, and the BET-specific surface areas were calculated to be 861.2 and $831.5 \text{ m}^2 \text{ g}^{-1}$, respectively. The slightly decreased specific surface area of **W2** may be due to the loading of cmrIr on the surface of the MOF. Fourier transform infrared spectroscopy (FT-IR) characterization was performed to determine the functional groups of **W1** and **W2**

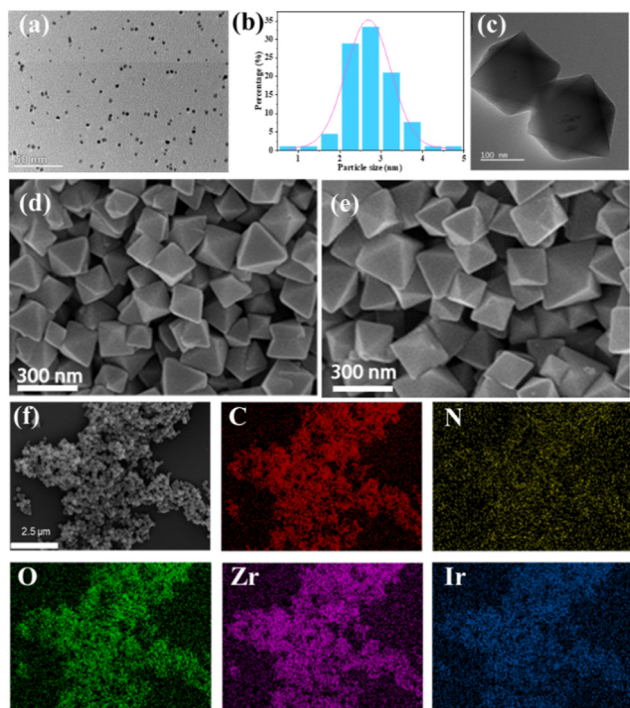


Fig. 2 (a) TEM images of Pt nanoparticles. (b) Particle size distribution of Pt nanoparticles. TEM (c) and SEM (d) images of **W1**. (e) SEM images of **W2**. (f) EDS image of **W2**.

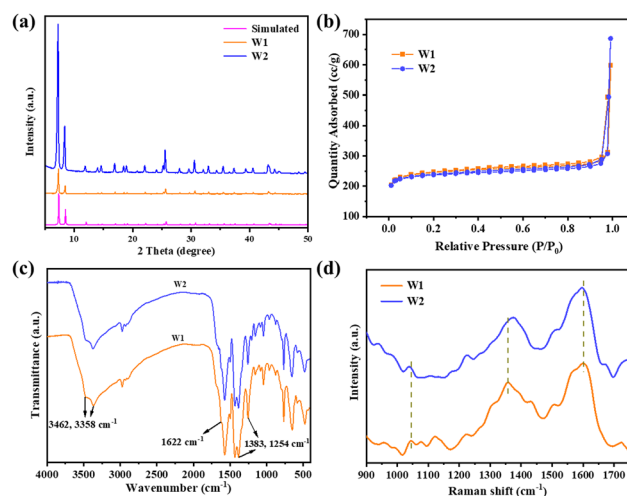


Fig. 3 (a) XRD curves of **W1**, **W2**, and standard UiO-66-NH_2 . (b) Nitrogen adsorption-desorption curves for **W1** and **W2** at 77 K. Infrared (c) and Raman (d) spectra of **W1** and **W2**.



(Fig. 3c). The absorption peaks at 3462 cm^{-1} , 3358 cm^{-1} , and 1622 cm^{-1} for **W1** correspond to the asymmetric and symmetric stretching vibrations of the amino group in the MOF ligand, while the absorption peaks at 1383 cm^{-1} and 1254 cm^{-1} correspond to the C–N stretching vibrations in the aryl ring. The infrared curves of **W2** are almost identical to those of **W1**. Due to the small grafting amount, cmrIr was not detected. Therefore, Raman tests were further performed (Fig. 3d). Compared to the Raman spectra of **W1**, the three peaks at 1600, 1361 and 1045 cm^{-1} showed slight shifts after grafting the cmrIr, which corresponded to 1596, 1376, and 1039 cm^{-1} in the curves of **W2**, respectively. This result proved that the carboxylate of cmrIr coordinates with the unsaturated site of **W1**, which leads to a change in its geometrical configuration.

X-ray photoelectron spectroscopy (XPS) characterization of cmrIr, **W1** and **W2** were performed and the results are shown in Fig. 4a. The peaks at 65.5 eV and 62.5 eV can be clearly seen in the high-resolution Ir 4f spectrum of the cmrIr powder, which corresponds to Ir 4f_{5/2} and Ir 4f_{7/2}, respectively. Similarly, the peaks at 65.4 eV and 62.4 eV can be seen in the high-resolution Ir 4f spectrum of **W3**, demonstrating the presence of Ir on the surface of **W2**. The slight shift of the double peak results from the change in the electronic environment of the Ir center.^{41–44} In addition, according to the high-resolution Zr 3d spectrum of **W1** (Fig. 4b), the peaks at 185.4 eV and 183.0 eV can be attributed to Zr 3d_{3/2} and Zr 3d_{5/2}, respectively. Compared to **W1**, the Zr 3d peak of **W2** is slightly shifted to 185.2 eV and 182.8 eV, which is attributed to the coordination of cmrIr to the Zr clusters that affect the electronic environment around Zr.^{22,26,45} The coordination bonds between cmrIr and Zr clusters provide a channel for electrons transferring from cmrIr to UiO-66-NH₂ and Pt, which facilitates electron migration. According to the ICP-MS results, the percentage of Ir element on the surfaces of **W2** is only 0.2% (Table S2, ESI[†]), which corresponds to the result of EDS.

The photocatalytic hydrogen evolution performance of **W2** was studied. UiO-66-NH₂ and **W1** were used as references. The photocatalytic performance was tested throughout 5 h using the synthesized MOF-based materials as catalysts, triethanolamine (5 mL) as a sacrificial agent, and DMF and H₂O (v/v = 54/1 mL) as solvents. Control experiments showed that hydrogen could not be detected in the system without the addition of a catalyst (**W1** or **W2**). As shown in Fig. 5a, UiO-66-NH₂ cannot achieve

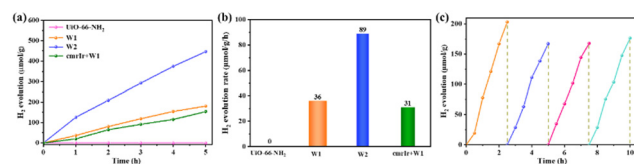


Fig. 5 Hydrogen evolution curves for UiO-66-NH₂, **W1**, **W2**, and cmrIr + **W1** (a), and the average rate of evolution for 5 h (b). (c) Cyclic stability test curves for **W2**.

hydrogen evolution under the test conditions, and the hydrogen evolution amount of **W1** is $180.7\text{ }\mu\text{mol g}^{-1}$. Surprisingly, after surface modification of cmrIr, **W2** evolved hydrogen at $446.4\text{ }\mu\text{mol g}^{-1}$, which is about 2.5 times that of **W1**. Meanwhile, as a control, we also put in cmrIr and **W1** with equal iridium and platinum contents as those in **W2** according to the test results of ICP-MS. And the amount of hydrogen evolution in 5 h is only $153.48\text{ }\mu\text{mol g}^{-1}$, which indicates that hybridizing iridium(III) complexes with MOFs could sensitize the MOF catalyst, and significantly enhance the activity of the MOF catalyst. It is deduced that there is a strong interaction between the iridium(III) complexes and the MOF. In addition, the average hydrogen evolution rate of the different samples is calculated over 5 h. As shown in Fig. 5b, the hydrogen evolution rate of **W1** is $36\text{ }\mu\text{mol g}^{-1}\text{ h}^{-1}$, and the hydrogen evolution rate of **W2** is enhanced to $89\text{ }\mu\text{mol g}^{-1}\text{ h}^{-1}$. The above photocatalytic test results indicate that the modification of iridium(III) complexes on the MOF surface contributes to the enhancement of photocatalytic hydrogen production.

The stability of **W2** was investigated by photocatalytic cycling tests, and the experimental results are shown in Fig. 5c. Four cycles of the photocatalytic test were carried out, and the hydrogen evolution activities of the second, third, and fourth cycles remained the same, but slightly lower than the first cycle. It is speculated that a part of cmrIr was physically adsorbed on the surface of **W2**, which detached from the surface of **W2** and dissolved into the photocatalytic solution after the first cycle of photocatalysis, so the photocatalytic activity slightly decreased in the subsequent cycle. To prove this, **W2** after photocatalysis was characterized and the results are shown in Fig. S12 (ESI[†]). After photocatalysis, the morphology of **W2** remained unchanged, which was individual octahedrons with sharp angles. The XRD curves were also the same as those before photocatalysis, which indicates that its crystallinity was unchanged, and **W2** had good stability. Nevertheless, XPS results show that the proportion of iridium elements on the surface of **W2** decreased from 0.2% to 0.14%, which could explain the slight decrease in hydrogen evolution activity after the first cycle.

To further investigate the origin of the high photocatalytic performance of **W2**, the photocurrent response and electrochemical impedance of **W1** and **W2** were tested. As shown in Fig. 6a, **W1** and **W2** exhibit periodic and stable photocurrent under the on and off of the lamp, with a photocurrent intensity of about $0.006\text{ }\mu\text{A}$ for **W3** and only about $0.0025\text{ }\mu\text{A}$ for **W1**. The photocurrent intensity of **W2** is about 2.5 times that of **W1**, indicating that **W2** has better electron-hole separation ability. As shown in Fig. 6b, **W2** shows a smaller radius of the Nyquist

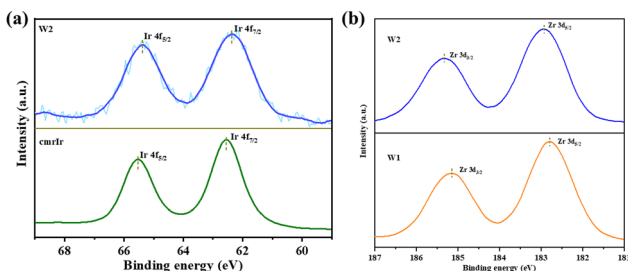


Fig. 4 (a) Ir 4f high-resolution XPS spectra of cmrIr and **W2**; (b) Zr 3d high-resolution XPS spectra of **W1** and **W2**.



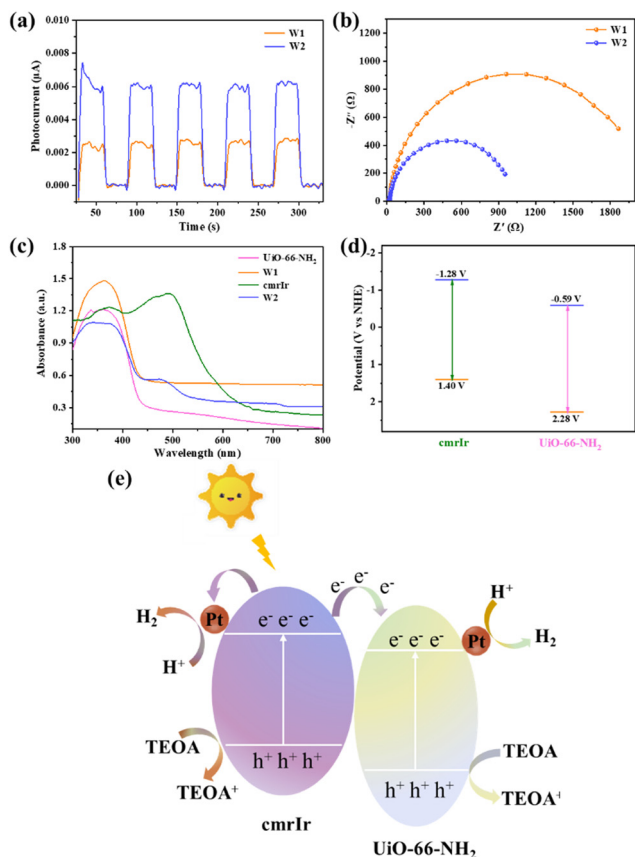


Fig. 6 Photocurrent response (a) and electrochemical impedance (b) curves for **W1** and **W2**. (c) Solid-state UV-visible diffuse reflectance spectra of UiO-66-NH₂, **W1**, cmrIr, and **W2**. (d) Potentiometric maps of cmrIr and UiO-66-NH₂. (e) Photocatalytic mechanism diagram of **W2**.

circle than **W1**, indicating that **W2** has a smaller interface transfer resistance when transferring electrons with other components. Solid-state UV diffuse reflectance characterization of the samples was performed to determine the light absorption capacity and the energy gap of the samples (Fig. 6c). CmrIr absorbs visible light well and its energy gap is only 2.14 eV, which is in general agreement with the data from the liquid absorption spectra described above (Fig. S13, ESI†). UiO-66-NH₂ and **W1** have almost no absorption in the visible region, and their energy gaps are 2.87 and 2.80 eV, respectively. In contrast to **W1**, **W2** has a new absorption peak at 450–500 nm and a significantly narrower energy gap of 2.24 eV. This result indicates that the introduction of cmrIr can significantly improve and broaden the visible light absorption of the MOF materials. Therefore, the enhanced photocatalytic performance of **W2** compared to **W1** can be attributed to its more visible light absorption and more efficient separation of electrons and holes as well as smaller interfacial transfer resistance, which makes it easier to trigger the photocatalytic reaction and facilitate the subsequent transfer of electrons.^{27,46}

The photocatalytic mechanism of **W2** was explored by performing electrochemical tests on the samples, and the Mott-Schottky curve of UiO-66-NH₂ is shown in Fig. S14 (ESI†). According to the calculation, the conduction band of UiO-66-

NH₂ was -0.59 V vs. NHE. The valence band value of UiO-66-NH₂ was calculated from the band gap value obtained from the solid-state UV test, which is 2.28 V vs. NHE. Unlike the MOFs, the electron gaining and losing ability of metallic iridium(III) complexes upon photoexcitation needs to be measured in terms of the excited-state redox potential. The excited state redox potential of cmrIr was determined and calculated using cyclic voltammetry (Fig. S15 and Table S3, ESI†). As shown in Fig. 6d, the excited state oxidation potential (E_{ox}^*) and excited state reduction potential (E_{red}^*) of cmrIr are -1.28 V and 1.40 V vs. NHE, respectively. After photoexcitation, the excited state oxidation potential of cmrIr is more negative than the conduction band of UiO-66-NH₂, which makes it easy to achieve electron transfer from the complex to MOF. Therefore, the photocatalytic process of **W2** is deduced as follows (Fig. 6e): under light illumination, both cmrIr and UiO-66-NH₂ absorb light energy to form the separation of electrons and holes, and UiO-66-NH₂ achieves hydrogen evolution only by transferring the electrons to the Pt nanoparticles. In contrast, **W2** has two electron transfer paths, one of which can directly transfer to Pt nanoparticles to achieve hydrogen evolution, and the other one is transferred to UiO-66-NH₂ and then to Pt nanoparticles to achieve hydrogen evolution, and this path promotes the separation of electrons and holes.

Conclusions

In this work, the iridium(III) complex with excellent light-absorbing properties was immobilized onto the MOF *via* coordination. Photocatalytic tests show that the hydrogen evolution activity of the MOFs was enhanced after modification of the iridium(III) complex, and the inherent photostability of the MOF was retained. This is due to the fact that the introduction of an iridium(III) complex to the MOFs can improve the visible light absorption ability of the material and promote electron-hole separation and transfer. This work is a preliminary exploration, demonstrating that even introducing extremely low content of iridium(III) complex on the MOF surface can significantly improve the hydrogen evolution activity. While taking into account the stability of the material, it can be a potential candidate for efficient and stable photocatalysts.

Experimental section

The synthesis of cmrIr

CmrIr was synthesized by the following process

Synthesis of iridium dichloro bridged compound [Ir(cmr)₂Cl]₂. 1,5-Cyclooctadiene iridium dichloride (1 g, 1.49 mmol) and coumarin 6 (2.09 g, 5.97 mmol) were added to a 100 mL single-neck round bottom flask with ethylene glycol ethyl ether (40 mL) as the solvent under argon protection, and the reactants were stirred at 150 °C for 6 h. As the reaction proceeded, the reactants in the system were dissolved and an orange solid was formed. After the reaction, the system was cooled to room temperature and filtered, and the filter cake was rinsed with



ethanol and petroleum ether in sequence. Without further purification, it was dried under a vacuum at 80 °C to obtain orange solid powder $[\text{Ir}(\text{cmr})_2\text{Cl}]_2$.

The synthesis of the auxiliary ligand L1. The auxiliary ligand **L1** was synthesized according to the method in the literature using a classic Suzuki coupling reaction. The specific process is as follows: 5,5'-dibromo-2,2'-bipyridine (2.0004 g, 6.375 mmol), 4-methoxycarbonylphenylboronic acid (3.4425 g, 19.125 mmol), and tetrakis(triphenylphosphine)palladium (0.75 g, 0.65 mmol) were added to a 120 mL thick-walled pressure tube. Subsequently, tetrahydrofuran (54 mL) and a pre-prepared potassium carbonate aqueous solution (2.5 M, 12 mL) were added. Under argon protection, the mixture was stirred at 80 °C for 72 hours. As the reaction progressed, a white solid gradually appeared in the reaction system. After the reaction was completed, it was cooled to room temperature, and filtered, and the filter cake was washed with tetrahydrofuran, water, and ethanol successively. It was dried under vacuum at 80 °C and a total of 2.3 g of white solid was obtained with a yield of 85%. ^1H NMR (400 MHz, CF_3COOD): δ 9.52 (d, J = 1.7 Hz, 1H), 9.14 (dd, J = 8.5, 2.0 Hz, 1H), 8.93 (d, J = 8.5 Hz, 1H), 8.54 (d, J = 8.3 Hz, 2H), 8.10 (d, J = 8.4 Hz, 2H), 4.31 (s, 3H). MS: m/z = 425.1.

The synthesis of the auxiliary ligand L2. The auxiliary ligand **L2** was obtained by hydrolysis of **L1** as follows. **L1** (0.3 g, 0.71 mmol) was added to a 100 mL single-necked round-bottomed flask with tetrahydrofuran (10 mL) and ethanol (10 mL) as solvents, followed by the addition of an aqueous solution of sodium hydroxide (3 M, 10 mL) to the system and the reaction was carried out at 70 °C overnight. At the end of the reaction, it was cooled to room temperature, the pH was adjusted to 1 with concentrated hydrochloric acid, extracted with ethyl acetate/water, and the organic phases were combined and dried with anhydrous sodium sulfate overnight. The filtrate was filtered and spun-dried, and the target product was dried under vacuum at 80 °C to give 0.24 g of white solid in 86% yield. ^1H NMR (400 MHz, CF_3COOD): δ 9.44 (d, J = 1.6 Hz, 1H), 9.06 (dd, J = 8.4, 1.9 Hz, 1H), 8.85 (d, J = 8.5 Hz, 1H), 8.51 (d, J = 8.3 Hz, 2H), 8.02 (d, J = 8.3 Hz, 2H). MS: m/z = 396.1.

The synthesis of the complex $[\text{Ir}(\text{cmr})_2(\text{L2})]^+$ (cmrIr). Auxiliary ligand **L2** (0.2376 g, 0.6 mmol), triethylamine (2 mL), and ethylene glycol ethyl ether (12 mL) were added to a 120 mL thick-walled pressure-resistant tube, and the reactants were stirred at 100 °C under the protection of argon gas for 1 h. After being cooled down to room temperature, ethylene glycol was added to $[\text{Ir}(\text{cmr})_2\text{Cl}]_2$ (0.5553 g, 0.3 mmol)-ethyl ether (30 mL) suspension in the argon environment, and the suspension was stirred at 150 °C for 5 days. At the end of the reaction, the suspension was cooled to room temperature, the pH was adjusted to 1 with 60% hexafluorophosphoric acid, and then the product was extracted with dichloromethane/water and dried with anhydrous sodium sulfate overnight. The suspension was filtrated, and the filtrate was then collected and dried by spin-drying. The obtained solid was finally dissolved with dichloromethane and purified by column chromatography

using methanol as eluent. After spin-drying the solvent, an orange target product was obtained. The product was dried under vacuum at 80 °C, and a total of 0.14 g of solid was obtained in 18% yield. ^1H NMR (400 MHz, DMSO-d_6): δ 8.90 (s, 1H), 8.67 (d, J = 8.6 Hz, 1H), 8.59 (d, J = 8.4 Hz, 1H), 8.08 (d, J = 7.8 Hz, 1H), 8.00 (d, J = 8.2 Hz, 2H), 7.55 (d, J = 8.2 Hz, 2H), 7.55 (d, J = 8.2 Hz, 2H), 8.00 (d, J = 8.2 Hz, 2H). 7.55 (d, J = 8.3 Hz, 2H), 7.23 (t, J = 7.8 Hz, 1H), 7.00 (t, J = 8.4 Hz, 1H), 6.51 (s, 1H), 6.27 (d, J = 8.5 Hz, 1H), 6.21–6.08 (m, 2H), 3.27 (d, J = 7.6 Hz, 4H), 0.95 (s, 4H), 0.95 (m, 2H), 0.05 (s, 1H), 0.05 (s, 1H), 0.05 (s, 1H), 0.05 (s, 1H), 0.05 (m, 1H) 4H, 0.95 (t, J = 7.0 Hz, 6H). ^{13}C NMR (101 MHz, DMSO-d_6): δ 181.89, 177.32, 168.05, 157.62, 155.24, 153.68, 153.00, 147.75, 147.08, 140.82, 139.30, 134.25, 132.36, 131.13, 130.44, 128.26, 126.56, 125.21, 125.02, 124.69, 121.80, 119.09, 116.64, 110.28, 44.47, 12.84. MS: m/z = 1287.3 (M^+).

Preparation of Pt nanoparticles

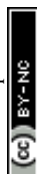
Pt nanoparticles were prepared by referring to the literature method. Chloroplatinic acid hexahydrate (0.0508 g) and poly(vinylpyrrolidone) with an average molecular weight of 55 000 (0.222 g) were quickly added to a 120 mL thick-walled pressure-resistant tube, and the system was subjected to ultrasonic stirring for 30 min until the solution exhibits a clarified orange color. Then the solution was heated at 180 °C with rapid stirring for 10 min, during which the solution was gradually changed from transparent to black. At the end of the reaction, the solution was cooled to room temperature with stirring, and 100 mL of acetone was added to the reaction solution to wash out the excess polyvinylpyrrolidone. The black oily platinum nanoparticles were obtained by precipitation and centrifugation of the solution for 5 minutes (8000 rpm), which were ultrasonically dispersed in DMF solvent (10 mL) and stored under refrigeration.

Preparation of Pt@UiO-66-NH₂ (W1)

Pt@UiO-66-NH₂ (**W1**) was prepared by referring to the literature method. ZrCl_4 (0.102 g, 0.43 mmol) and acetic acid (6 mL) and 25 mL DMF were added to a 100 mL beaker and sonicated for 30 min until the solids were completely dissolved, which was designated as solution A. 2-Aminoterephthalic acid (0.0725 g, 0.4 mmol) and 25 mL DMF were added to a 100 mL beaker, and sonicated for 30 min until the solids were completely dissolved, which was designated as solution B. After mixing solutions A and B and continuing to sonicate for 30 min, the pre-made platinum nanoparticles (2 mL) were added to the mixed solution, and the solution was heated at 12 °C for 24 h. At the end of the reaction, the reaction solution was cooled to room temperature, and centrifuged. The clear liquid was discarded, and the solid obtained was washed with DMF and methanol, and dried under vacuum at 80 °C to obtain Pt@UiO-66-NH₂ (**W1**). The preparation method of UiO-66-NH₂ was the same as that of **W1**, but only without the addition of platinum nanoparticles during the process of preparation.

Preparation of cmrIr/Pt@UiO-66-NH₂ (W2)

CmrIr (0.2574 g, 0.2 mmol), trifluoroacetic acid (300 μL) and DMF (25 mL) were added to a 100 mL beaker, and ultrasonically



dissolved. Then **W1** (0.3 g) was added to the system, and ultrasonically dispersed for 30 minutes. The system was heated at 120 °C for 60 hours. At the end of the reaction, the system was cooled to room temperature, and centrifuged. The resulting solid was washed with DMF and methanol in turn, and dried under vacuum at 80 °C to obtain iridium(III)-based MOF hybrid material cmrIr/Pt@UiO-66-NH₂ (**W2**).

Photocatalytic hydrogen evolution experiment

Photocatalytic hydrogen evolution experiments were carried out in a vacuum-tight glass pipeline. In this case, the MOF and its hybrid material were the catalyst (20 mg), triethanolamine (5 mL) was the sacrificial agent, and the solvent system included DMF (54 mL) and water (1 mL). The photocatalytic pretreatment included the following operations. An appropriate amount of catalyst was weighed and added to the mixed solution, and after sonication for 5 min to disperse uniformly, nitrogen was passed into the solution under stirring for 30 min. Subsequently, the reaction tank was connected to a glass line and evacuated (40 min). A xenon lamp was used for continuous irradiation, the solution was continuously stirred and the temperature was precisely controlled at 6 °C by water cooling. The gas is automatically fed into a gas chromatograph, which is connected to the vacuum-tight glass line for online analysis.

Cycling experiments. The same feeding volume as above was tested, and four rounds of cycling experiments were carried out; at the end of each round the system is emptied and re-vacuumed (30 min).

Photoelectrochemical tests

The redox potential of the iridium(III) complexes was tested by cyclic voltammetry under the following conditions. A three-electrode system was used, with a glassy carbon electrode as the working electrode (5 mm in diameter), which was polished with alumina polishing powder, a saturated mercuric glycol electrode as the reference electrode, and a platinum wire electrode as the counter electrode, and a 0.1 M tetrabutylammonium hexafluorophosphate acetonitrile solution as the electrolyte (ready-to-use). Tetrabutylammonium hexafluorophosphate needs to be recrystallized before preparation and the solvent used is ethanol. The system needs to be deoxidized before testing each sample.

The photocurrent response, electrochemical impedance, and Mott-Schottky tests were also performed using a three-electrode system, *i.e.*, working electrode, reference electrode and counter electrode. Commercially available silver/silver chloride electrodes and platinum sheet electrodes were chosen as the reference electrode and counter electrode, respectively. The working electrode was prepared as follows: MOF material (2 mg) was added to an ethanol solution (1 mL) containing Nafion (10 µL), dispersed homogeneously. 200 µL of the suspension was dripped on an FTO conductive glass (1 × 1 cm²) and then dried under an infrared lamp. 0.2 M aqueous sodium sulfate solution was used as the electrolyte. For photocurrent response testing, the working electrode was exposed to intermittent light from a 300 W xenon lamp. The electrochemical

impedance test is performed in the dark and under nitrogen. For the Mott Schottky test, the frequency of the reference electrode was varied and the three frequencies selected were 500 Hz, 1000 Hz and 1500 Hz.

Author contributions

All authors have contributed significantly. Yue Wang and Pengyang Deng conceived and designed the experiment. Yue Wang conducted the main experiments and data analysis, and Yifan Huang participated in the data analysis. Yifan Huang, Yifan Zhang, and Pengyang Deng led the paper writing, and Shihan Liu and Shuaichuan Cui contributed to the text. Pengyang Deng and Yifan Zhang supervised the project. All authors agree with the content of the manuscript.

Conflicts of interest

The authors declare no conflicts of interest.

Acknowledgements

This work was supported by the National Natural Science Foundation of China (no. 51803208) and the Youth Innovation Promotion Association CAS (E2202005).

Notes and references

- 1 R. M. Bullock, J. G. Chen, L. Gagliardi, P. J. Chirik, O. K. Farha, C. H. Hendon, C. W. Jones, J. A. Keith, J. Klosin, S. D. Minter, R. H. Morris, A. T. Radosevich, T. B. Rauchfuss, N. A. Strotman, A. Vojvodic, T. R. Ward, J. Y. Yang and Y. Surendranath, Using nature's blueprint to expand catalysis with Earth-abundant metals, *Science*, 2020, **369**(6505), eabc3183.
- 2 A. Fujishima and K. Honda, Electrochemical Photolysis of Water at a Semiconductor Electrode, *Nature*, 1972, **238**(5358), 37–38.
- 3 Z. Jiang, X. Xu, Y. Ma, H. S. Cho, D. Ding, C. Wang, J. Wu, P. Oleynikov, M. Jia, J. Cheng, Y. Zhou, O. Terasaki, T. Peng, L. Zan and H. Deng, Filling metal-organic framework mesopores with TiO₂ for CO₂ photoreduction, *Nature*, 2020, **586**(7830), 549–554.
- 4 S. Cao, T.-S. Chan, Y.-R. Lu, X. Shi, B. Fu, Z. Wu, H. Li, K. Liu, S. Alzuabi, P. Cheng, M. Liu, T. Li, X. Chen and L. Piao, Photocatalytic pure water splitting with high efficiency and value by Pt/porous brookite TiO₂ nanoflutes, *Nano Energy*, 2020, **67**, 104287.
- 5 J. Kosco, S. Gonzalez-Carrero, C. T. Howells, T. Fei, Y. Dong, R. Sougrat, G. T. Harrison, Y. Firdaus, R. Sheelamantula, B. Purushothaman, F. Moruzzi, W. Xu, L. Zhao, A. Basu, S. De Wolf, T. D. Anthopoulos, J. R. Durrant and I. McCulloch, Generation of long-lived charges in organic semiconductor heterojunction nanoparticles for efficient



- photocatalytic hydrogen evolution, *Nat. Energy*, 2022, **7**(4), 340–351.
- 6 W. Wang, Y. Li, Z. Kang, F. Wang, J. C. Yu and A. NIR-driven, photocatalyst based on α -NaYF₄:Yb,Tm@TiO₂ core-shell structure supported on reduced graphene oxide, *Appl. Catal., B*, 2016, **182**, 184–192.
 - 7 J. Fu, J. Yu, C. Jiang and B. Cheng, g-C₃N₄-Based Heterostructured Photocatalysts, *Adv. Energy Mater.*, 2018, **8**(3), 1701503.
 - 8 C. F. Fu, X. Wu and J. Yang, Material Design for Photocatalytic Water Splitting from a Theoretical Perspective, *Adv. Mater.*, 2018, **30**(48), e1802106.
 - 9 R. Li, Y. Weng, X. Zhou, X. Wang, Y. Mi, R. Chong, H. Han and C. Li, Achieving overall water splitting using titanium dioxide-based photocatalysts of different phases, *Energy Environ. Sci.*, 2015, **8**(8), 2377–2382.
 - 10 N. Lu, X. Yan, H. Kobayashi, W. Liu, S. Chen, S. Liang, J. Zhang and R. Li, Oxygen-mediated water splitting on metal-free heterogeneous photocatalyst under visible light, *Appl. Catal., B*, 2020, **279**, 119378.
 - 11 J. Pang, R. G. Mendes, A. Bachmatiuk, L. Zhao, H. Q. Ta, T. Gemming, H. Liu, Z. Liu and M. H. Rummeli, Applications of 2D MXenes in energy conversion and storage systems, *Chem. Soc. Rev.*, 2019, **48**(1), 72–133.
 - 12 T. Takata, J. Jiang, Y. Sakata, M. Nakabayashi, N. Shibata, V. Nandal, K. Seki, T. Hisatomi and K. Domen, Photocatalytic water splitting with a quantum efficiency of almost unity, *Nature*, 2020, **581**(7809), 411–414.
 - 13 D. Kim, D. R. Whang and S. Y. Park, Self-Healing of Molecular Catalyst and Photosensitizer on Metal-Organic Framework: Robust Molecular System for Photocatalytic H₂ Evolution from Water, *J. Am. Chem. Soc.*, 2016, **138**(28), 8698–8701.
 - 14 F. Song, C. Wang and W. Lin, A chiral metal-organic framework for sequential asymmetric catalysis, *Chem. Commun.*, 2011, **47**(29), 8256–8258.
 - 15 J. Zhang, T. Bai, H. Huang, M. H. Yu, X. Fan, Z. Chang and X. H. Bu, Metal-Organic-Framework-Based Photocatalysts Optimized by Spatially Separated Cocatalysts for Overall Water Splitting, *Adv. Mater.*, 2020, **32**(49), e2004747.
 - 16 Z. Zhuang and D. Liu, Conductive MOFs with Photophysical Properties: Applications and Thin-Film Fabrication, *Nano-Micro Lett.*, 2020, **12**(1), 132.
 - 17 C. A. Kent, D. Liu, L. Ma, J. M. Papanikolas, T. J. Meyer and W. Lin, Light harvesting in microscale metal-organic frameworks by energy migration and interfacial electron transfer quenching, *J. Am. Chem. Soc.*, 2011, **133**(33), 12940–12943.
 - 18 L. Liu, S. Du, Y. Xiao, X. Guo, S. Jin, G. Shao and F. Zhang, Saturated Ti-coordinated {001} facets-dependent photocatalytic water reduction over NH₂-MIL-125(Ti) sheets: Observation and unraveling of facets effect, *Appl. Catal., B*, 2023, **338**, 123094.
 - 19 P. Ayala, S. Naghdi, S. P. Nandan, S. N. Myakala, J. Rath, H. Saito, P. Guggenberger, L. Lakhanlal, F. Kleitz, M. C. Toroker, A. Cherevan and D. Eder, The Emergence of 2D Building Units in Metal-Organic Frameworks for Photocatalytic Hydrogen Evolution: A Case Study with COK-47, *Adv. Energy Mater.*, 2023, **13**(31), 2300961.
 - 20 H. Li, M. Eddaoudi, M. O'Keeffe and O. M. Yaghi, Design and synthesis of an exceptionally stable and highly porous metal-organic framework, *Nature*, 1999, **402**(6759), 276–279.
 - 21 W. Wang, X. Xu, W. Zhou and Z. Shao, Recent Progress in Metal-Organic Frameworks for Applications in Electrocatalytic and Photocatalytic Water Splitting, *Adv. Sci.*, 2017, **4**(4), 1600371.
 - 22 X. Ma, L. Wang, Q. Zhang and H. L. Jiang, Switching on the Photocatalysis of Metal-Organic Frameworks by Engineering Structural Defects, *Angew. Chem., Int. Ed.*, 2019, **58**(35), 12175–12179.
 - 23 C. Gomes Silva, I. Luz, F. X. Llabres i Xamena, A. Corma and H. Garcia, Water stable Zr-benzenedicarboxylate metal-organic frameworks as photocatalysts for hydrogen generation, *Chem*, 2010, **16**(36), 11133–11138.
 - 24 X. He, Y. Ding, Z. Huang, M. Liu, M. Chi, Z. Wu, C. U. Segre, C. Song, X. Wang and X. Guo, Engineering a Self-Grown TiO₂/Ti-MOF Heterojunction with Selectively Anchored High-Density Pt Single-Atomic Cocatalysts for Efficient Visible-Light-Driven Hydrogen Evolution, *Angew. Chem., Int. Ed.*, 2023, **62**(25), e202217439.
 - 25 C. Wang, K. E. deKrafft and W. Lin, Pt nanoparticles@photoactive metal-organic frameworks: efficient hydrogen evolution via synergistic photoexcitation and electron injection, *J. Am. Chem. Soc.*, 2012, **134**(17), 7211–7214.
 - 26 J. D. Xiao, Q. C. Shang, Y. J. Xiong, Q. Zhang, Y. Luo, S. H. Yu and H. L. Jiang, Boosting Photocatalytic Hydrogen Production of a Metal-Organic, *Angew. Chem., Int. Ed.*, 2016, **55**(32), 9389–9395.
 - 27 K. Sun, M. Liu, J. Pei, D. Li, C. Ding, K. Wu and H. L. Jiang, Incorporating Transition-Metal Phosphides Into Metal-Organic Frameworks for Enhanced Photocatalysis, *Angew. Chem., Int. Ed.*, 2020, **59**(50), 22749–22755.
 - 28 C. Wang, Z. Xie, K. E. DeKrafft and W. Lin, Doping metal-organic frameworks for water oxidation, carbon dioxide reduction, and organic photocatalysis, *J. Am. Chem. Soc.*, 2011, **133**(34), 13445–13454.
 - 29 Q. Wang and D. Astruc, State of the Art and Prospects in Metal-Organic Framework (MOF)-Based and MOF-Derived Nanocatalysis, *Chem. Rev.*, 2020, **120**(2), 1438–1511.
 - 30 J. He, J. Wang, Y. Chen, J. Zhang, D. Duan, Y. Wang and Z. Yan, A dye-sensitized Pt@UiO-66(Zr) metal-organic framework for visible-light photocatalytic hydrogen production, *Chem. Commun.*, 2014, **50**(53), 7063–7066.
 - 31 L. Liu, H. Meng, Y. Chai, X. Chen, J. Xu, X. Liu, W. Liu, D. M. Guldi and Y. Zhu, Enhancing Built-in Electric Fields for Efficient Photocatalytic Hydrogen Evolution by Encapsulating C₆₀ Fullerene into Zirconium-Based Metal-Organic Frameworks, *Angew. Chem., Int. Ed.*, 2023, **62**(11), e202217897.
 - 32 S. Y. Han, D. L. Pan, H. Chen, X. B. Bu, Y. X. Gao, H. Gao, Y. Tian, G. S. Li, G. Wang, S. L. Cao, C. Q. Wan and G. C. Guo, A Methylthio-Functionalized-MOF Photocatalyst with High Performance for Visible-Light-Driven H₂ Evolution, *Angew. Chem., Int. Ed.*, 2018, **57**(31), 9864–9869.



- 33 M. A. Syzgantseva, C. P. Ireland, F. M. Ebrahim, B. Smit and O. A. Syzgantseva, Metal Substitution as the Method of Modifying Electronic Structure of Metal-Organic Frameworks, *J. Am. Chem. Soc.*, 2019, **141**(15), 6271–6278.
- 34 Y.-F. Chen, L.-L. Tan, J.-M. Liu, S. Qin, Z.-Q. Xie, J.-F. Huang, Y.-W. Xu, L.-M. Xiao and C.-Y. Su, Calix[4]arene based dye-sensitized Pt@UiO-66-NH₂ metal-organic framework for efficient visible-light photocatalytic hydrogen production, *Appl. Catal., B*, 2017, **206**, 426–433.
- 35 S. Mao, J. W. Shi, G. Sun, Y. Zhang, D. Ma, K. Song, Y. Lv, J. Zhou, H. Wang and Y. Cheng, PdS Quantum Dots as a Hole Attractor Encapsulated into the MOF@Cd(0.5)Zn(0.5)S Heterostructure for Boosting Photocatalytic Hydrogen Evolution under Visible Light, *ACS Appl. Mater. Interfaces*, 2022, **14**, 48770–48779.
- 36 S. Mao, Y. Zou, G. Sun, L. Zeng, Z. Wang, D. Ma, Y. Guo, Y. Cheng, C. Wang and J. W. Shi, Thio linkage between CdS quantum dots and UiO-66-type MOFs as an effective transfer bridge of charge carriers boosting visible-light-driven photocatalytic hydrogen production, *J. Colloid Interface Sci.*, 2021, **581**, 1–10.
- 37 S. Mao, J.-W. Shi, G. Sun, Y. Zhang, X. Ji, Y. Lv, B. Wang, Y. Xu and Y. Cheng, Cu (II) decorated thiol-functionalized MOF as an efficient transfer medium of charge carriers promoting photocatalytic hydrogen evolution, *Chem. Eng. J.*, 2021, **404**, 126533.
- 38 S. Mao, J.-W. Shi, G. Sun, D. Ma, C. He, Z. Pu, K. Song and Y. Cheng, Au nanodots@thiol-UiO66@ZnIn2S4 nanosheets with significantly enhanced visible-light photocatalytic H₂ evolution: The effect of different Au positions on the transfer of electron-hole pairs, *Appl. Catal., B*, 2021, **282**, 119550.
- 39 J. Wang, Y. Liu, Y. Li, L. Xia, M. Jiang and P. Wu, Highly Efficient Visible-Light-Driven H₂ Production via an Eosin Y-Based Metal-Organic Framework, *Inorg. Chem.*, 2018, **57**(13), 7495–7498.
- 40 S. Guo, L. H. Kong, P. Wang, S. Yao, T. B. Lu and Z. M. Zhang, Switching Excited State Distribution of Metal-Organic Framework for Dramatically Boosting Photocatalysis, *Angew. Chem., Int. Ed.*, 2022, **61**(30), e202206193.
- 41 J. Wang, X. Liu, C. Li, M. Yuan, B. Zhang, J. Zhu and Y. Ma, Fabrication of perylene imide-modified NH₂-UiO-66 for enhanced visible-light photocatalytic degradation of tetracycline, *J. Photochem. Photobiol., A*, 2020, **401**, 112795.
- 42 G. Jin, J. Liu, C. Wang, W. Gu, G. Ran, B. Liu and Q. Song, Ir nanoparticles with multi-enzyme activities and its application in the selective oxidation of aromatic alcohols, *Appl. Catal., B*, 2020, **267**, 118725.
- 43 X. X. Wang, D. A. Cullen, Y. T. Pan, S. Hwang, M. Wang, Z. Feng, J. Wang, M. H. Engelhard, H. Zhang, Y. He, Y. Shao, D. Su, K. L. More, J. S. Spendelow and G. Wu, Nitrogen-Coordinated Single Cobalt Atom Catalysts for Oxygen Reduction in Proton Exchange Membrane Fuel Cells, *Adv. Mater.*, 2018, **30**(11), 1706758.
- 44 X. Zhao, Y. Zhang, X. Zhao, X. Wang, Y. Zhao, H. Tan, H. Zhu, W. Ho, H. Sun and Y. Li, Urea and Melamine Formaldehyde Resin-Derived Tubular g-C₃N₄ with Highly Efficient Photocatalytic Performance, *ACS Appl. Mater. Interfaces*, 2019, **11**(31), 27934–27943.
- 45 Z. X. Cai, Z. L. Wang, Y. J. Xia, H. Lim, W. Zhou, A. Taniguchi, M. Ohtani, K. Kobi, T. Fujita and Y. Yamauchi, Tailored Catalytic Nanoframes from Metal-Organic Frameworks by Anisotropic Surface Modification and Etching for the Hydrogen Evolution Reaction, *Angew. Chem., Int. Ed.*, 2021, **60**(9), 4747–4755.
- 46 P. Wang, S. Guo, H. J. Wang, K. K. Chen, N. Zhang, Z. M. Zhang and T. B. Lu, A broadband and strong visible-light-absorbing photosensitizer boosts hydrogen evolution, *Nat. Commun.*, 2019, **10**(1), 3155.

